Analysis of Water Management in Proton Exchange Membrane Fuel Cells[*]

BAO Cheng (包　成), OUYANG Minggao (欧阳明高)[**], YI Baolian (衣宝廉)[†]

State Key Laboratory of Automotive Safety and Energy, Tsinghua University, Beijing 100084, China;
†Dalian Institute of Chemical Physics, Chinese Academy of Sciences, Dalian 116023, China

Abstract: A two-dimensional, steady-state, isothermal water-management model for a complete proton exchange membrane fuel cell (PEMFC) was developed. The model includes the transport in the diffusion layer and the proton exchange membrane (PEM) with a pseudo-homogeneous model for the cathode catalyst layer. The predicted fuel cell performance with variable cathode porosities compares well with experimental results. The model is then used to investigate the effects of some structural parameters, such as the rib size, the interdigitated flow field, and various operating conditions including the gas flow rate, the cell temperature and pressure, humidification, and the relative humidity at the inlet. Water management is best achieved by tuning the anode operating conditions.

Key words: proton exchange membrane (PEM); fuel cells; water management; mathematical model

Introduction

Fuel cells provide an environmentally friendly high-efficiency power source that is not limited by the Carot efficiency. The proton exchange membrane fuel cell (PEMFC) is considered to be the most promising candidate for electric vehicles by virtue of its high power density, zero pollution, low operating temperature, quick startup capability, and long lifetime. PEMFC can also be used in distributed power systems, submarines, and aerospace applications.

Proper water management within the cell is essential to the proper operation of the PEMFC. Dehydration of the membrane results in increasing resistive losses, while excessive water leads to flooding of the cathode. Therefore, the water management within the PEMFC

involves walking a tightrope between these two extremes. Bernardi and Verbrugge[1] modeled the water transport and electrochemical behavior of the cell with the restriction of a fully hydrated membrane. Springer et al.[2] described the electro-osmotic drag and back diffusion mechanisms of the water transport and the net water transport coefficient in the membrane without the electrochemical reaction in the catalyst layer. However, their catalyst layer model is not well coupled with the other components[3]. One-dimensional models cannot simulate the important species concentration variations in the cross-section and flow directions. The pseudo two-dimensional models by Nguyen and Yi[4,5] analyzed the water distribution along the flow channel without the gas diffusion layer (GDL). Kazim et al.[6] compared the differences between a conventional and an interdigitated gas distributor. Similarly, Yi and Nguyen[7] analyzed the multi-component transport in the interdigitated flow field. Fuller and West[8] used concentrated solution theory[9] to analyze effects of the rib size on the fuel cell performance. The two-dimensional, two-phase models by He et al.[10] and

You et al.[11], Natarajan and Nguyen[12,13], and Wang et al.[14,15] considered the evaporation and condensation of the water. Due to the complexity of the two-phase phenomenon, these models focused on the cathode and did not explain the effects of anode operating conditions that significantly influence water management.

This article describes a two-dimensional, isothermal, steady-state water management model which includes all the structures in the PEMFC. The model is used to analyze the effects of various design and operating conditions and can be used to analyze the water management in a PEM fuel cell engine system.

1　Mathematical Model

Figure 1 shows a schematic of the domain that is a cross-section of a PEMFC. The model includes all the parts of the PEMFC except for the anode catalyst layer. The x-direction goes across the gas channel and the flow field with the y-direction parallel to the ion transport dimension. For the conventional gas distributor, the x direction consists of a shoulder and two halves of the inlet channel. For the interdigitated flow field, the upper part of the channel represents one half of the outlet channel. As shown in Fig. 1, the positive y direction is in the transport direction of the reactants and ions. The complexity of the fuel cell was simplified with the following assumptions:

1) The gas diffusion layers, catalyst layers, and membrane are all isotropic.

2) Only steady state is considered.

3) The cell temperature remains constant.

4) All species are in the gaseous phase and the phase change of water was not included. The gas mixture is an ideal gas.
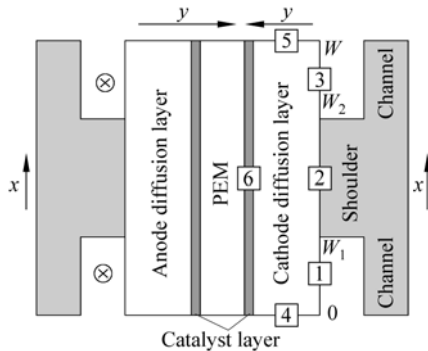

Fig. 1　Schematic of the modeled domain

5) For simplicity, the activation polarization and net water transport coefficient are constant along the x direction in an identical condition.

1.1　Governing equations

1.1.1　Flow channel equations
The species concentrations must satisfy continuity in the flow channel. The molar fraction of each species at the outlet of flow channel can be calculated from the hydrogen and air stoichiometric ratio and the net water transport coefficient as follows.

$$x_{w,a}^{out} = \frac{\xi_a \cdot x_{w,a}^{in} - 2\alpha(1 - x_{w,a}^{in})}{x_{w,a}^{in} - 2\alpha(1 - x_{w,a}^{in}) + \xi_a - 1} \tag{1}$$

$$x_{w,c}^{out} = \frac{\xi_c \cdot x_{w,c}^{in} + 0.42(1 + 2\alpha)(1 - x_{w,c}^{in})}{\xi_c + 0.21(1 + 4\alpha)(1 - x_{w,c}^{in})} \tag{2}$$

$$x_{O_2}^{out} = \frac{0.21(\xi_c - 1)(1 - x_{w,c}^{in})}{\xi_c + 0.21(1 + 4\alpha)(1 - x_{w,c}^{in})} \tag{3}$$

In the model, the arithmetical average of the inlet and outlet molar fractions is used as the boundary condition of the diffusion layer[16]. Natarajan and Nguyen[13] proved that the cell energy generation overestimated in the case inlet molar fraction is used. Therefore, the pseudo three-dimensional model can be reduced to a two-dimensional model.

1.1.2　Diffusion layers equations
Continuity:

$$\nabla \cdot (c\boldsymbol{u}) = 0 \tag{4}$$

Ideal gas law:

$$c = \frac{p}{RT} \tag{5}$$

Momentum (Darcy's law):

$$\boldsymbol{u} = -\frac{k_p}{\mu}\nabla p \tag{6}$$

Species conservation:

$$\nabla \cdot (cx_i\boldsymbol{u}) - \nabla \cdot (\varepsilon c D_i^{eff}\nabla x_i) = 0 \tag{7}$$

where the gas mixture viscosity is defined as

$$\mu = \frac{\sum x_i M_i^{1/2}\mu_i}{\sum x_i M_i^{1/2}} \tag{8}$$

The species conservation equation uses the species diffusivities in air in the cathode and the binary diffusivity of hydrogen in water vapor in the anode. The effective diffusion coefficients are obtained using the

Bruggemann correction in addition to their dependence on pressure and temperature,

$$D_i^{\text{eff}} = D_i \varepsilon^{1.5} \tag{9}$$

1.1.3   Equations of catalyst layer

Considering the anode catalyst layer to be an infinitely thin interface, the pseudo homogeneous model of the cathode catalyst layer is

$$\frac{dI(y)}{dy} = A_v i_0 \left(\frac{c_{O_2}}{c_{O_2}^{\text{ref}}} \right)^{\gamma} \left[\exp\left(\frac{a_c F \eta}{RT} \right) - \exp\left(\frac{-a_a F \eta}{RT} \right) \right] \tag{10}$$

$$\frac{dc_{O_2}}{dy} = \frac{1}{4FD_{O_2,\text{eff}}^{\text{cat}}} \left[I(y) - I \right] \tag{11}$$

$$\frac{d\eta}{dy} = \frac{1}{\kappa_{m,\text{eff}}^{\text{cat}}} I(y) \tag{12}$$

Equation (10) is the Butler-Volmer equation, Eq. (11) is Fick's first law, and Eq. (12) is Ohm's law. The effective diffusivity of oxygen in the catalyst layer is approximated using the series resistance of the oxygen flow through the membrane and the liquid water corrected by the Bruggemann method[17].

$$D_{O_2,\text{eff}}^{\text{cat}} = \frac{\phi^{3/2} D_{O_2,m} D_{O_2,H_2O}}{(1 - f_m) D_{O_2,m} + f_m D_{O_2,H_2O}} \tag{13}$$

Using the Nernst-Planck equation, the ionic conductivity is obtained by assuming that the membrane phase is fully hydrated in the cathode catalyst layer.

$$\kappa_m = \frac{F^2 c_f}{RT} D_{H^+} \tag{14}$$

$$\kappa_{m,\text{eff}}^{\text{cat}} = \left(f_m \phi \right)^{3/2} \kappa_m \tag{15}$$

1.1.4   Membrane equations

The water transport in the membrane includes the electro-osmotic drag and the back diffusion mechanisms and neglects the pressure gradient between the anode and the cathode. The net water transport coefficient is defined as the ratio of the net water flux in PEM to the ion flux. Although there are other theories[9,18] describing the dependence of the electro-osmotic drag on the membrane water content, a linear expression is used here. Springer described the dependence of the water diffusivity in the membrane on the water content and temperature[2].

$$n_{\text{drag}} = \frac{2.5}{22} \lambda \tag{16}$$

$$n_{\text{dif}} = D_w^m \frac{F}{I_{\text{avg}}} \frac{\rho_{m,\text{dry}}}{M_{m,\text{dry}}} \frac{d\lambda}{dy} \tag{17}$$

$$\alpha = n_{\text{drag}} - n_{\text{dif}} \tag{18}$$

where the average current density is

$$I_{\text{avg}} = \frac{1}{W} \int_0^W I \, dx \tag{19}$$

1.2   Boundary conditions

As shown in Fig. 1, the diffusion layer has six boundaries. At the inlet, boundaries 1 and 3 are the Dirichlet-type boundary conditions,

$$p = p_k, \quad x_i = x_i^{\text{ch}} = 0.5(x_i^{\text{in}} + x_i^{\text{out}}) \tag{20}$$

The no-slip boundary condition is used at the interface in contact with the shoulder of the gas distributor, boundary 2,

$$\frac{\partial p}{\partial y} = 0, \frac{\partial x_i}{\partial y} = 0 \tag{21}$$

Symmetry conditions are used at boundaries 4 and 5,

$$\frac{\partial p}{\partial x} = 0, \frac{\partial x_i}{\partial x} = 0 \tag{22}$$

At the electrode/catalyst layer interface, boundary 6, the species fluxes are related to the local current density by

$$N_{w,a} = \alpha \frac{I}{F}, N_{H_2} = \frac{I}{2F}, N_{O_2} = \frac{I}{4F},$$

$$N_{w,c} = -(1 + 2\alpha) \frac{I}{2F} \tag{23}$$

The catalyst layer boundary conditions are

$$c_{O_2} \big|_{y=0} = \frac{p x_{O_2}^{\text{cd}}}{H_{O_2}}, \quad I(y) \big|_{y=0} = 0, \quad I(y) \big|_{y=l_{\text{cat}}} = I \tag{24}$$

The membrane boundary conditions are defined by the vapor activity at the electrode/membrane interface[2],

$$a = \frac{p \bar{x}_{w,k}}{p_{\text{sat}}} \tag{25}$$

1.3   Numeric solution

The boundaries of components are coupled because of the net water transport coefficient. The two-point boundary problems in the membrane and the catalyst layer were solved using the Bvp4c algorithm of MATLAB. The partial differential equations in the diffusion layer were solved using FEMLAB. The

activation polarization was calculated from the average current density and electric load using the Newton-Raphson algorithm.

The cell activation polarization is obtained from the catalyst model:

$$\eta_{act} = \eta\big|_{y=l_{cat}} \tag{26}$$

The ohmic polarization was obtained from the relationship between the membrane resistance and the water content[2]:

$$\eta_{ohm} = I_{avg} \cdot \int_0^{l_m} \frac{dy}{\sigma(\lambda)} \tag{27}$$

The concentration polarization was obtained from Fick's law:

$$\eta_{conc} = \frac{RT}{2F} \ln\left(\frac{p_c x_{O_2}^{ch}}{p x_{O_2}^{cd}} \right) \tag{28}$$

The cell voltage at the open circuit potential was obtained from test data which included the effect of gas impurities and crossover:

$$V = V_{oc} - \eta_{act} - \eta_{ohm} - \eta_{conc} \tag{29}$$

2 Results and Discussion

2.1 Experimental validation and the base case

Table 1 lists the important parameter values used for the base case with a conventional gas distributor.

Figure 2 shows the oxygen and water vapor concentrations in the cathode gas diffusion layers and the local current density distribution for the base case. The oxygen concentration decreases and the water vapor concentration in the cathode increases along the positive y direction as oxygen consumed and water vapor is produced. The positive net water transport coefficient means the water moves from the anode to the cathode, so the molar fraction of water vapor in the anode is slightly less because of the higher binary diffusivity of hydrogen and water vapor. Because of the obstruction due to the shoulder, the oxygen transport to the reaction surface is restricted and the water movement is restricted along the x direction from the inlet to the middle of the shoulder. The water vapor movement at the anode is also restricted. Therefore, the maximum vapor concentration occurs on the reaction surface at the middle of the shoulder which is farthest from the inlet. The local current density distribution in Fig. 2d reflects

Table 1 Base case parameters

Open circuit voltage (V)	0.975
Average current density (A/cm²)	1.0
Gas diffuser thickness (cm)	0.03
Membrane thickness (cm)	0.005
Catalyst layer thickness (cm)	0.001
Half channel width (cm)	0.03
Shoulder width (cm)	0.055
Porosity of anode GDL	0.6
Porosity of cathode GDL	0.5
Air stoichiometric ratio	2.5
Hydrogen stoichiometric ratio	1.25
Air pressure (MPa)	0.3
Hydrogen pressure (MPa)	0.3
Cell temperature (℃)	70
Air humidification temperature (℃)	70
Hydrogen humidification temperature (℃)	70
Air inlet relative humidity (%)	100
Hydrogen inlet relative humidity (%)	100
Dry membrane density (kg/m³)	2000
Ionomer equivalent mass (kg/mol)	1.1
Ion concentration in PEM (mol/m³)	1200

the oxygen concentration distribution at the reaction interface and symmetry of the structure.

The predicted polarization curve is compared with experimental results in Fig. 3 with reasonable agreements obtained at low and moderate electric loads. The discrepancy between the model results with fixed porosity (0.5) and the test results for high current densities is due to condensation of the water vapor at the cathode so that the diffusion layer is partially flooded, which reduced the effective porosity of the cathode. Since the model did not consider the two-phase effects of the water, the cathode porosity was modified at different electric loads to approximate the flooding. For average current densities of 0.3, 1.0, and 1.5 A/cm², the cathode porosity was chosen as 0.6, 0.5, and 0.2. The porosities at other current densities were interpolated linearly from themselves. The dashed line in Fig. 3 shows the simulation results with the variable porosity. The three overpotentials are also plotted in Fig. 3.

Figure 4a shows the variation of the membrane water content and the net water transport coefficient for various average current densities. At higher electric loads, the anode-side membrane segment has much lower water content than in the cathode side, which
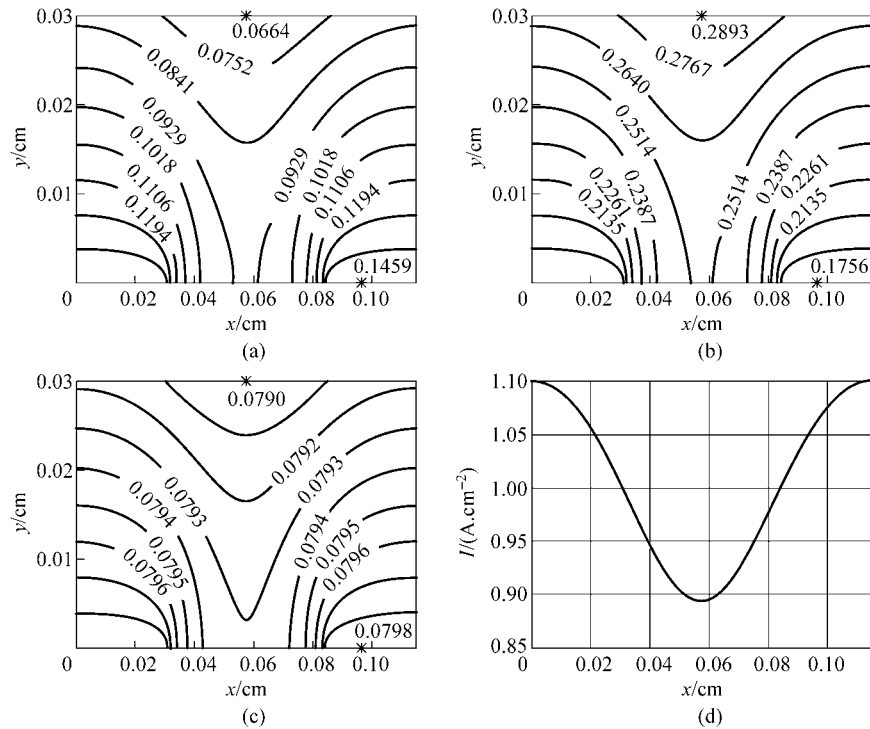
Fig. 2 Simulation results for the conventional flow field as the base case. (a), Oxygen molar fraction contours in the cathode GDL; (b), Water vapor molar fraction contours in the cathode GDL; (c), Water vapor molar fraction contours in the anode GDL; (d), Local current density distribution
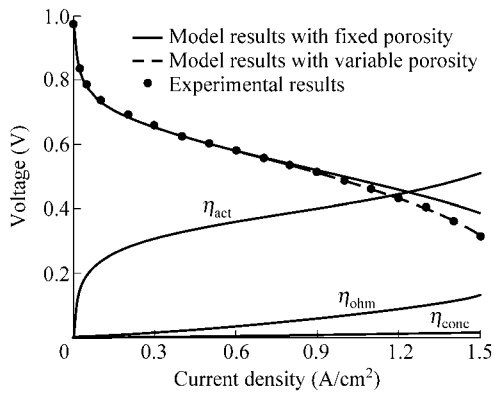

Fig. 3 Comparison of the predicted polarization curve with experimental results

agrees with Buchi's results[19]. The resistance of the membrane dominated by the anode-side water content increases even though the membrane is more hydrated. As the current density increases, the back diffusion mechanism does not offset the electro-osmotic drag effect, so the net water transport coefficient increases.

Figure 4b shows the oxygen concentration and ionic current density distribution at $x=0$ in the cathode catalyst layer. The ionic current increases to the maximum as the oxygen is consumed. At higher local current densities, I, the current density transfers more
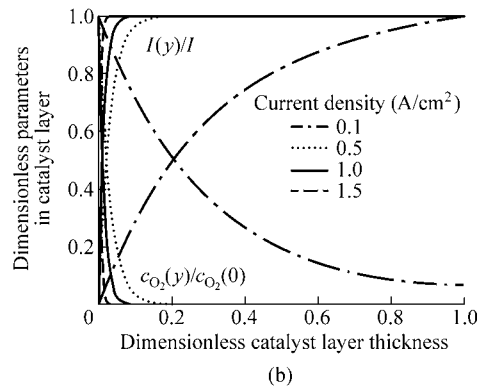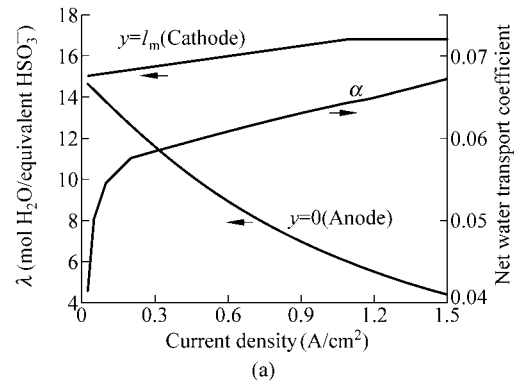

Fig. 4 Effects of average current density. (a), Water content at the membrane boundaries and net water transport coefficient; (b), Distribution of the dimensionless ionic current density and the oxygen concentration at $x=0$ in the cathode catalyst layer

rapidly from the solid phase to the membrane phase, so a larger fraction of the catalyst layer is inactive. As shown in Fig. 4b, the utilization of the catalyst layer is almost 5% in the base case.

2.2　Effects of structural parameters

The cell structure significantly affects the cell performance. Up to this point, the polarization has been a function of the cathode porosity. This section considers the interdigitated flow field and the size of the rib.

2.2.1　Effects of interdigitated flow field

The interdigitated gas distributor is a promising type of flow field that improves the cell performance[20].

For this analysis, the cathode flow field was replaced with an interdigitated flow field without changing the anode flow field.

In this case, boundary 1 in Fig. 1 is a Newman-type boundary condition[10,15],

$$p = p_c , \quad cx_i v - \varepsilon c D_i^{\text{eff}} \frac{\partial x_i}{\partial y} = cx_i^{\text{in}} v \qquad (30)$$

The full development boundary condition is used at the channel outlet, boundary 3,

$$p = p_{\text{out}} , \quad \frac{\partial x_i}{\partial y} = 0 \qquad (31)$$

As with the conventional case, the total oxygen balance is given by

$$\int_0^{W_1} (cx_{\text{O}_2} v - \varepsilon c D_{\text{O}_2}^{\text{eff}} \frac{\partial x_{\text{O}_2}}{\partial y})\Big|_{y=0} \, \mathrm{d}x +$$

$$\int_{W_2}^{W} (cx_{\text{O}_2} v - \varepsilon c D_{\text{O}_2}^{\text{eff}} \frac{\partial x_{\text{O}_2}}{\partial y})\Big|_{y=0} \, \mathrm{d}x = \int_0^{W} \frac{I}{4F} \mathrm{d}x \qquad (32)$$

Figure 5a shows the superficial velocity distribution in the cathode GDL. The gas flow changes its flow direction near the inlet and outlet areas through the diffusion layer. Above the shoulder, the gas velocity is nearly uniform due to the porous medium flow. To keep the same air stoichiometric ratio of 2.5 as for the base case, the pressure difference between the inlet and outlet was 230 Pa. The maximum velocity located in the outlet close to the shoulder is 9.28 cm/s. Figures 5b and 5c show the water vapor and oxygen contours. The oxygen concentration decreases and the water vapor concentration increases from the inlet to the outlet. As a result, the oxygen diffusion to the catalyst interface is in the same direction as the gas flow above the inlet
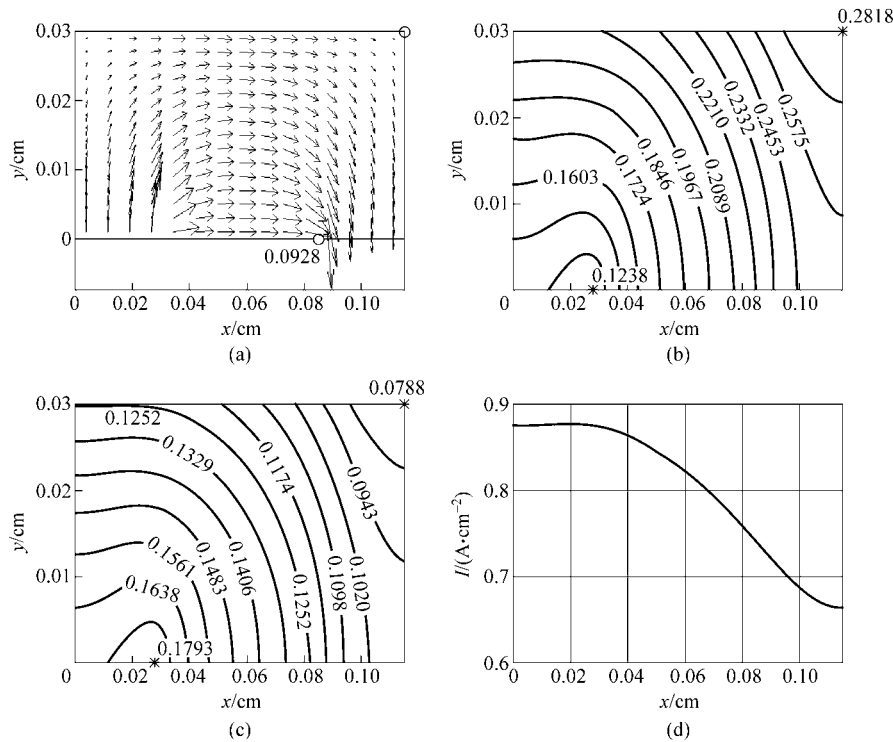

Fig. 5　Simulation results for the interdigitated cathode flow field with the other parameters the same as for the base case. (a), Gas flow superficial velocities; (b), Water vapor molar fraction; (c), Oxygen molar fraction; (d), Local current density distribution

but they flow in opposite directions above the outlet. Compared to the vapor concentration field for the conventional gas distributor shown in Fig. 2b, though the maximum vapor concentrations are almost identical, the average vapor molar fraction is 0.2349 for the interdigitated flow field which is smaller than 0.2775 for the base case because the gas transport is mainly due to convection mechanism in the interdigitated flow field instead of the diffusion in the conventional case, which improves the water removal. The actual channel and shoulder sizes in this simulation were almost half those of Yi's[7]. The benefits of the interdigitated gas distributor will be more obvious as the number of channels is decreased. Figure 5d shows the local current density distribution, where the activation overpotential, 0.39 V, is smaller than the value of 0.4122 V in the conventional case.

2.2.2   Effects of shoulder size

Figure 6a shows the effects of shoulder size with a fixed channel width. The wider shoulders increase the gas transport distance to the reaction surface. So for the same average current density, the local current density distribution is less even for the larger shoulder fractions in the modeling domain. Increasing the shoulder width from 0.02 to 0.12 cm increases the corresponding activation overpotential from 0.3987 to 0.4299 V for I_{avg}=1 A/cm^2. Similarly, a wider shoulder also restricts the water removal. Although this makes the membrane more hydrated and reduces the resistance loss, the water accumulation will flood the GDL especially at high electric loads.

Figure 6b shows the effects of the number of channels for a fixed channel-to-shoulder ratio. It maintains the symmetry in Fig. 1 with three different designs. For a given domain size, more channels mean a smaller shoulder and channel. As the channel and shoulder sizes reduce, the gas mass transport distance is shortened which results in the smaller activation polarization and more uniform distribution of the local current density. The utilization of the reactive area above the shoulder is also enhanced.

Although the smaller rib size is preferred, the shoulder is the only part of the current collector in contact with the GDL, so a small rib results in a high contact resistance. So these two effects must be balanced to give an optimum shoulder size.
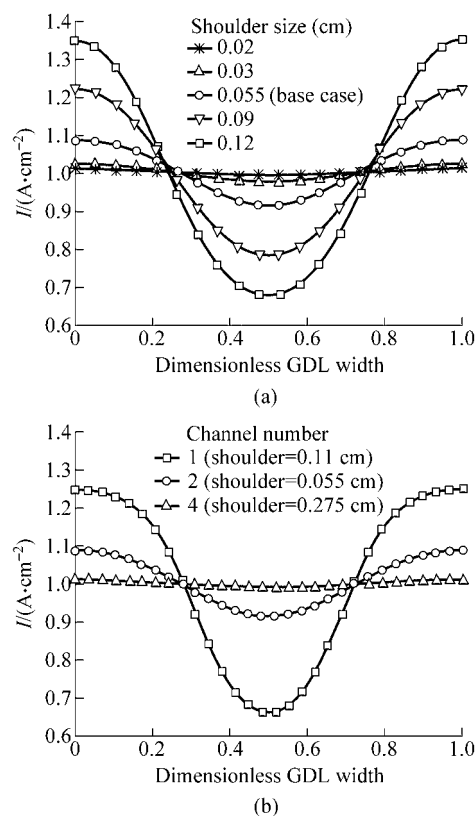

Fig. 6   Effects of shoulder size on the current density distribution as I_{avg}=1 A/cm^2. (a), fixed channel width; (b), fixed channel-to-shoulder ratio

2.3   Effects of the operating conditions

Any factor influencing the state of the reaction gas will affect the cell performance. As each parameter is varied, the other parameters are kept constant at the values in the base case listed in Table 1. The cathode porosity is constant at 0.5 for simplicity.

2.3.1   Effect of air stoichiometric ratio

The air flow rate is one of the most important factors affecting the cell performance. Figure 7 shows the effects of air stoichiometric ratio on the cell voltage and the water transport. The cell voltage increases with increasing air stoichiometric ratio. Equation (2) shows that the molar vapor fraction is reduced in the outlet for higher stoichiometric ratios, so the water vapor activities on both sides of the membrane are reduced and the membrane is somewhat dehydrated. Because the membrane is very thin and the inlet gases are all fully humidified, the net water transport coefficient remains almost constant. Thus, more power can be generated with little effect on the water management.

However, since the air stream to the PEM fuel cell

engine is from an air compressor or blower, higher air flow rates require more power, so there is an optimum flow rate which gives the highest system efficiency.
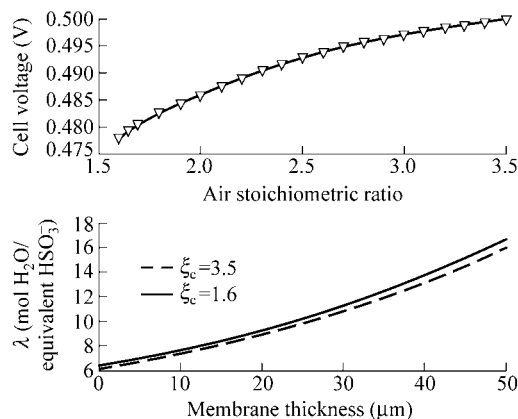

Fig. 7   Effect of air stoichiometric ratio for I_{avg}= 1 A/cm^2

2.3.2   Effect of hydrogen stoichiometric ratio

The hydrogen stoichiometric ratio has less influence on the polarization, but it has significant effect on the water management. As shown in Fig. 8a, when the hydrogen in the inlet is saturated with water vapor (relative humidity is 1), as the hydrogen stoichiometric ratio increases and the membrane becomes more hydrated, the electro-osmotic drag increases. The reduced membrane water content gradient then reduces the back diffusion, so the net water transport coefficient is increased.

Compared to the air stoichiometric ratio, the influence of the hydrogen stoichiometric ratio on the water transport is more related to the humidification. As shown in Fig. 7, even if the relative humidity of the air is unity, the membrane still dehydrates as the air stoichiometric ratio is increased because of the inert nitrogen in the cathode gas. Figure 8b shows that the variation of the water transport with dry hydrogen is the opposite of that shown in Fig. 8a for wet hydrogen. As the anode flow rate increases, the membrane becomes dehydrated and the intense back diffusion mechanism causes water transport from the cathode to the anode.

During cell operation, flooding of the electrode must be avoided especially at high current densities. The results show that larger flow rates at both the anode and the cathode can remove the water in the GDL. However, a dryer, higher flow-rate anode feed stream is more effective since it has little influence on cell polarization, and a large anode flow rate is easily
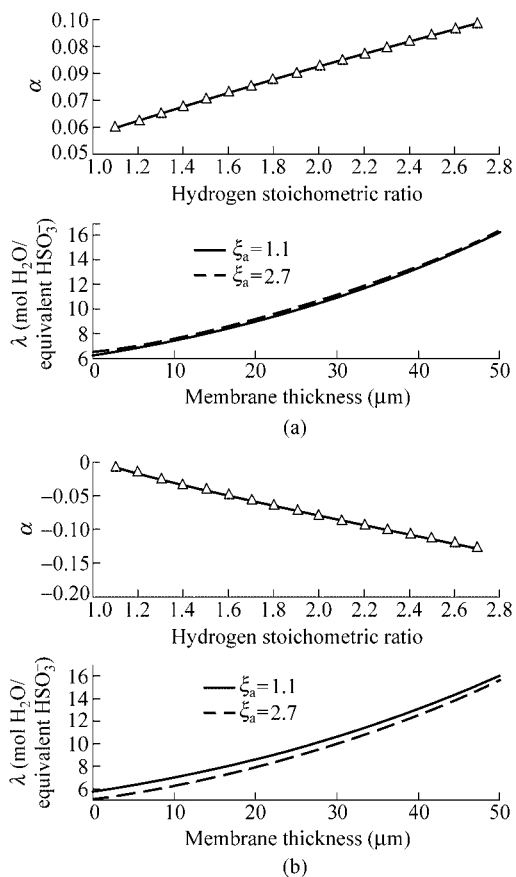

Fig. 8   Effects of hydrogen stoichiometric ratio as I_{avg}=1 A/cm^2. (a), Air relative humidity is 1; (b), Air relative humidity is 0

realized with a recirculating hydrogen pump or a blower which requires relatively little power. The anode water removal method of Ballard is a typical application[21].

2.3.3   Effect of pressure

Figure 9 shows the effects of pressure on cell performance. As the pressure increases, the higher oxygen concentration reduces the reaction overpotential. In addition, the increased partial pressure of water vapor makes the membrane more hydrated. As shown in Fig. 9, though more water enhances the electro-osmotic drag, the increased water content gradient makes the back diffusion mechanism strong enough to reduce the net water transport coefficient.

Note that the anode and cathode pressure are assumed to be identical here. In practice, the pressure gradient between the anode and the cathode can increase permeation of water through the membrane, so the pressure difference can be used to give the best net water transport coefficient in a PEMFC.
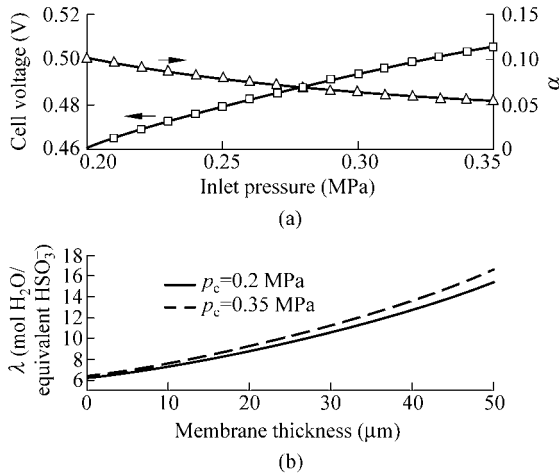
Fig. 9   Effect of inlet gas pressure for I_{avg}=1 A/cm² with no pressure gradient between the anode and the cathode

2.3.4   Effect of the cell temperature

Figure 10 shows the effects of cell temperature. As the cell temperature increases, the higher water vapor saturation pressure tends to reduce the water activity on both sides of the membrane. At the same time, the enhanced diffusivity increases the water vapor molar fraction in the anode and decreases it in the cathode. The general result is that the water vapor activity in the anode side is increased and the total water content in the cathode side is increased. In addition to the lower resistance loss, the less activation overpotential resulting from the higher exchange current density[8] greatly increases the cell voltage.

$$i_0 = i_0^{ref} \exp\left[\frac{73.2 \times 10^3}{R} \left(\frac{1}{T^{ref}} - \frac{1}{T} \right) \right] \qquad (33)$$
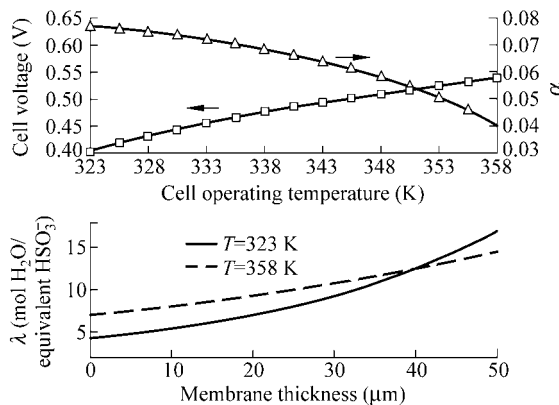

Fig. 10   Effect of the cell temperature for I_{avg}=1 A/cm²

The increased water content and the decreased gradient reduce the net water transport coefficient, because the water diffusivity in the membrane increases

exponentially relative to the temperature while the electro-osmotic drag coefficient is linearly dependent on the membrane water content[2]. Therefore, the back diffusion mechanism is enhanced enough to offset the increased electro-osmotic drag as the cell temperature is increased.

2.3.5   Effect of humidification

Figure 11 shows the effect of the anode humidification temperature on the water transport. As the anode humidification temperature (T_a) increases, the water content in the membrane increases especially on the anode side. The intensified electro-osmotic drag and the weakened back diffusion increase the water transport from the anode to the cathode. Although the ohmic loss is reduced, the cell voltage varies little because of the very thin membrane and the fast electrochemical reaction in the anode.
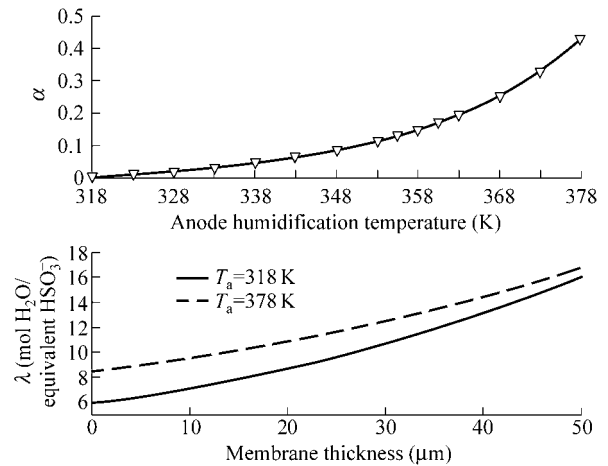

Fig. 11   Effect of anode humidification temperature for I_{avg}=1 A/cm²

The effects of the cathode humidification temperature, the anode inlet relative humidity, and the cathode inlet relative humidity were similar to that of T_a. The humidification in the anode should be used for water management because of the dominant dependence of the ohmic losses on the anode-side conditions.

3   Conclusions

A two-dimensional, isothermal, steady-state water management model for a complete PEMFC is presented.

1) The pseudo three-dimensional model was reduced to a two-dimensional model by averaging the inlet and outlet species concentrations.

2) When variable cathode diffusion layer porosities were used to model the effect of flooding, the predicted polarization curve agreed well with experimental results. The model can be used for cell design, including the analysis of the effect of rib size, the benefits of interdigitated flow field, and the utilization of the catalyst layer.

3) The model was used to analyze the effects of the operating conditions such as cell temperature, pressure, flow rate, and humidification. The results show that water management can best be controlled by regulating the operating conditions in the anode.

4) The model cannot distinguish the co-flow and counter-flow modes, the effects of temperature gradient and two-phase flow which should be considered in the future work.

Acknowledgements

Nomenclature

a	water vapor activity
a_a	anode transport coefficient
a_c	cathode transport coefficient
A_v	catalyst surface area per unit volume (m^2/m^3)
c	molar concentration (mol/m^3)
c_f	ion concentration in the membrane (mol/m^3)
D	diffusivity (m^2/s)
f_m	membrane phase fraction in the cathode catalyst layer
F	Faraday constant (96 487 C/mol)
H	Henry's law constant (Pa · m^3/mol)
i_0	exchange current density (A/m^2)
I	current density (A/m^2)
k_p	permeability of porous diffusion layer (m^{-2})
l	thickness (m)
M	molecular mass (kg/mol)
n	water transport coefficient
N	molar flux ($mol/(m^2 · s)$)
p	pressure (Pa)
R	universal gas constant (8.3143 J/(mol · K))
T	temperature (K)
T_k	humidification temperature (K)
$\boldsymbol{u}$	velocity vector (m/s)
v	y-direction velocity component (m/s)
V	voltage (V)

W	width (m)
x	species molar fraction
x, y	x and y directions
$\overline{}$	average along the x direction

Greek symbols

α	net water transport coefficient
λ	water content in membrane (mol H_2O/equivalent HSO_3^{-1})
ε	diffusion layer porosity
κ	conductivity ($\Omega^{-1} · m^{-1}$)
σ	membrane conductivity considering partial hydration ($\Omega^{-1} · m^{-1}$)
η	polarization (V)
ϕ	void fraction of catalyst layer
ρ	density (kg/m^3)
μ	dynamic viscosity (kg/(m · s))
ξ	stoichiometric ratio

Superscripts and subscripts

a	anode
act	activation
avg	average
c	cathode
cat	catalyst layer
cd	interface of diffusion layer and catalyst layer
ch	channel
conc	concentration
dif	diffusion
drag	electro-osmotic drag
eff	effective property that accounts for porosity
H_2O	liquid water
i	species
in	flow channel inlet
k	a or c
m	membrane
O_2	oxygen
oc	open circuit
ohm	ohmic
out	flow channel outlet
ref	reference
sat	saturated water vapor
w	water vapor

References

[1]　Bernardi D M, Verbrugge M W. A mathematical model of the solid-polymer-electrolyte fuel cell. *J. Electrochem.*

Soc., 1992, **139**(9): 2477-2491.

[2] Springer T E, Zawodzinski T A, Gottesfeld S. Polymer electrolyte fuel cell model. *J. Electrochem. Soc.*, 1991, **138**(8): 2334-2342.

[3] Springer T E, Zawodzinski T A, Wilson M S, Gottesfeld S. Characterization of polymer electrolyte fuel cells using AC impedance spectroscopy. *J. Electrochem. Soc.*, 1996, **143**(2): 587-599.

[4] Nguyen T V, White R E. A water and heat management model for proton exchange membrane fuel cells. *J. Electrochem. Soc.*, 1993, **140**(8): 2178-2186.

[5] Yi J S, Nguyen T V. An along-the-channel model for proton exchange membrane fuel cells. *J. Electrochem. Soc.*, 1998, **145**(4): 1149-1159.

[6] Kazim A, Liu H T, Forges P. Modeling of performance of PEM fuel cells with conventional and interdigitated flow fields. *J. Applied Electrochem.*, 1999, **29**(12): 1409-1416.

[7] Yi J S, Nguyen T V. Multicomponent transport in porous electrodes of proton exchange membrane fuel cells using the interdigitated gas distributors. *J. Electrochem. Soc.*, 1999, **146**(1): 38-45.

[8] West A C, Fuller T F. Influence of rib spacing in proton-exchange-membrane electrode assemblies. *J. Applied Electrochem.*, 1996, **26**(6): 557-565.

[9] Fuller T F, Newman J. Water and thermal management in solid-polymer-electrolyte fuel cells. *J. Electrochem. Soc.*, 1993, **140**(5): 1218-1225.

[10] He W, Yi J S, Nguyen T V. Two-phase flow model of the cathode of PEM fuel cells using interdigitated flow fields. *AIchE J.*, 2000, **46**(10): 2053-2064.

[11] You L, Liu H. A two-phase flow and transport model for the cathode of PEM fuel cells. *Int. J. Heat and Mass Transfer*, 2002, **45**(13): 2277-2287.

[12] Natarajan D, Nguyen T V. A two-dimensional, two-phase, multicomponent, transient model for the cathode of a proton exchange membrane fuel cell using conventional gas distributors. *J. Electrochem. Soc.*, 2001, **148**(12): A1324-A1335.

[13] Natarajan D, Nguyen T V. Three-dimensional effects of liquid water flooding in the cathode of a PEM fuel cell. *J. Power Sources*, 2003, **115**(1): 66-80.

[14] Wang Z H, Wang C Y, Chen K S. Two-phase flow and transport in the air cathode of proton exchange membrane fuel cells. *J. Power Source*s, 2001, **94**(1): 40-50.

[15] Wang Z H, Wang C Y. Two-phase flow and transport in the interdigitated air cathode of proton exchange membrane fuel cells. In: HTD-Vol. 366-1, Proceedings of the ASME, Heat Transfer Division 2000. Orlando, Florida, 2000: 27-33.

[16] Springer T E, Wilson M S, Gottesfeld S. Modeling and experimental diagnostics in polymer electrolyte fuel cells. *J. Electrochem. Soc.*, 1993, **140**(12): 3513-3526.

[17] Marr Curtis, Li Xianguo. Composition and performance modeling of catalyst layer in a proton exchange membrane fuel cell. *J. Power Sources*, 1999, **77**(1): 17-27.

[18] Eikerling M, Kharkats Y I, Kornyshev A A, Volfkovich Y M. Phenomenological theory of electro-osmotic effect and water management in polymer electrolyte proton-conduction membranes. *J. Electrochem. Soc.*, 1998, **145**(8): 2684-2699.

[19] Buchi F N, Scherer G G. Investigation of the transversal water profile in Nafion membranes in polymer electrolyte fuel cells. *J. Electrochem. Soc.*, 2001, **148**(3): A183-A188.

[20] Wood D L III, Yi J S, Nguyen T V. Effect of direct liquid water injection and interdigitated flow field on the performance of proton exchange membrane fuel cells. *Electrochimica Acta*, 1998, **43**(24): 3795-3809.

[21] Voss H H, Wilkinson D P, Pickup P G, Johnson M C, Basura V. Anode water removal: A water management and diagnostic technique for solid polymer membrane fuel cells. *Electrochimica Acta*, 1995, **40**(3): 321-328.